

Scientific Research Associates, inc.

50 Nye Road, P.O. Box 1058
Glastonbury, Connecticut 06033
(203) 659-0333

AD-A198 836

VALIDATION OF A FORWARD MARCHING PROCEDURE TO COMPUTE
TIP VORTEX GENERATION PROCESS FOR SHIP PROPELLER BLADES

by

F.J. de Jong, T.R. Govindan, R. Levy and S.J. Shamroth
Scientific Research Associates, inc.
Glastonbury, CT 06033

DTIC
ELECTE
SEP 20 1988
S D

Final Report R88-920023-F
Prepared under Contract N00014-84-C-0661

for
Department of the Navy
Office of Naval Research

August 1988

DEFENSE
Approved
Date

88 9 6 14 2

ABSTRACT

The tip vortex flow field has a significant influence on the performance of a ship propeller. The ability to compute the tip vortex flow field would be a valuable aid in the design of ship propellers, and in the analysis of their performance. The present report demonstrates the feasibility of computing the tip vortex generation process with a forward-marching computation procedure. For the purpose of this study, turbulent flow test cases were considered. The results of the computations were compared with experimental data from Gray et al. (Ref. 1), and demonstrate the capability of the forward-marching procedure to accurately compute the flow processes in the tip vortex generation. The flow field is computed from a set of three-dimensional viscous flow equations with no empiricism introduced for the vorticity generated and shed at the propeller tip. (JES) ↗



Approved For	
THIS FORM	<input checked="" type="checkbox"/>
OTHER	<input type="checkbox"/>
REVISION	<input type="checkbox"/>
By <i>per ltr</i>	
Date	
A-1	

TABLE OF CONTENTS

Nomenclature	ii
1. Introduction	1
2. The Forward Marching Computation Procedure for Ship Propeller Tip Flow Fields	2
2.1 Primary-Secondary Velocity Decomposition	3
2.2 Surface Potential Equations	4
2.3 Streamwise Momentum	5
2.4 Secondary Velocity	5
2.5 Pressure Equation	6
2.6 The Gas Law Equation.....	7
2.7 Turbulence Model	7
2.8 Governing System of Equations.....	8
2.9 Numerical Method	9
2.10 Summary of Algorithm.....	9
2.11 Boundary Conditions for the Tip Vortex Flow Computations.....	11
3. Results.....	13
3.1 The Inviscid Flow Calculations.....	13
3.2 The Viscous Flow Calculation for 6.18° Incidence	15
3.3 Data Comparison for 6.18° Incidence	16
3.4 Computed Results for 11.4° Incidence	18
3.5 Additional Results Downstream of the Trailing Edge	19
4. Conclusions.....	20
Acknowledgement.....	21
References.....	23
Figures.....	

NOMENCLATURE

c	Blade chord
c_p	Pressure coefficient
\bar{F}	Force due to viscous stress (Eq. 10)
\hat{i}_n	Unit vector normal to transverse coordinate surface
\hat{i}_p	Primary flow direction
\hat{i}_1, \hat{i}_2	Orthonormal vectors in the transverse coordinate surface
p	Static pressure
\bar{R}	Force due to a rotating coordinate system (Eq. 10)
Re	Reynolds number
\bar{U}	Velocity vector
U_p	Primary flow velocity
\bar{U}_s	Secondary flow velocity vector
\bar{V}_s	Known vector field in the transverse coordinate surfaces (e.g. the transverse component of an inviscid flow velocity vector field)
V_t	Tangential component of the \bar{V}_s and ϕ -contributions to the secondary velocity at a solid boundary.
x	Distance from the blade leading edge
x_1, x_2, x_3	Coordinates in the \hat{i}_1 -, \hat{i}_2 -, and \hat{i}_n - direction, respectively
α	Angle of incidence of the blade
ρ	Density
ρ_0	Reference density (constant)
ϕ	Scalar potential (Eq. 3)
ψ	Vector surface potential (Eq. 3)
Ω_n	Secondary vorticity, i.e., vorticity based on the secondary flow within the transverse surfaces (Eq. 7)
∇	Gradient operator
∇_s	Surface gradient operator (Eq. 4)

1. INTRODUCTION

The tip vortex flow field plays a significant role in the performance of a ship propeller. The low pressure region found at the center of a tip vortex may lead to cavitation. The presence of cavitation in the flow field has serious consequences in terms of structural, acoustic and performance considerations. A better understanding of the tip vortex generation process and a method of analyzing the tip vortex flow field would provide valuable help in the design of ship propellers.

The flow field in the tip region is complex, three-dimensional, and viscous, with large secondary velocities. A qualitative picture of the tip region flow field in a cross-section normal to the primary flow direction is shown in Fig. 1. As can be seen here, the transverse velocity along the tip changes direction in the vicinity of the tip vortex, a phenomenon commonly referred to as cross-flow separation. The large secondary velocities and the occurrence of cross-flow separation preclude the possibility of using conventional boundary layer solution techniques to compute the tip vortex flow field. On the other hand, a solution of the full Navier-Stokes equations that adequately resolves the tip vortex flow field would require formidable computational resources. A more economical approach is the use of an approximate set of three-dimensional viscous flow equations which is applicable to the tip vortex flow field but which does not require the resources needed for the solution of the full Navier-Stokes equations. The parabolized Navier-Stokes equations discussed in Section 2 represent such a set. These equations contain in them all the physical processes of tip vortex generation and can be solved economically by forward marching procedures.

The attractive possibility of using a forward-marching procedure to compute the tip vortex generation process was first examined by Shamroth and Briley (Ref. 2), and more recently by Lin et al. (Ref. 3) and Govindan et al. (Ref. 4). This report provides a quantitative assessment of the validity of this procedure for the tip vortex analysis. With the focus being on the computation of the vortex generation process, effects of blade leading and trailing edges and hub effects were neglected. The test cases were chosen to allow a data comparison to be made. Thus, geometry consisted of a straight blade with an NACA 0012 airfoil section and a rounded tip (a half-body of revolution, see Fig. 2). The results of the turbulent flow calculations were

compared with experimental surface pressure measurements in the tip region by Gray et al. (Ref. 1). A brief outline of the forward-marching procedure and a discussion of the results of the computation of the vortex generation process are presented in this report.

2. THE FORWARD MARCHING COMPUTATION PROCEDURE FOR SHIP PROPELLER TIP FLOW FIELDS

The forward marching computation procedure used for the solution of the parabolized Navier-Stokes equations provides an economical and accurate method for computing many three-dimensional viscous flow fields. This procedure, initially developed for internal flow fields (Refs. 5-7), has been extended to the computation of the ship propeller tip flow field. The governing equations and the computational scheme are presented in this section. This procedure is capable of considering both fixed and rotating coordinate systems.

Governing equations are derived through approximations made relative to a curvilinear coordinate system fitted to and aligned with the flow geometry under consideration. The coordinate system is chosen such that the streamwise or marching coordinate either coincides with or is at least approximately aligned with a known inviscid primary flow direction as determined, for example, by a potential flow for the given geometry. Transverse coordinate surfaces must be approximately perpendicular to solid walls or bounding surfaces, since diffusion is permitted only in these transverse coordinate surfaces.

Equations governing the primary flow velocity U_p and a secondary vorticity Ω_n normal to transverse coordinate surfaces are derived utilizing approximations which permit solution of the governing equations as an initial-value problem, provided reversal of the composite streamwise velocity does not occur. Terms representing diffusion normal to transverse coordinate surfaces (in the streamwise direction) are neglected. The pressure gradient term that appears in the streamwise momentum equation is assumed known (for example from an a priori potential flow solution for the geometry under consideration). Secondary flow velocities are determined from scalar and vector surface potential calculations in transverse coordinate surfaces, once the primary velocity and secondary vorticity are known. With the computed velocity field, the pressure field associated with the velocity field can be determined. For

compressible flow, an equation is added for the density, and for high Reynolds number flows, a turbulence model is specified.

2.1 Primary-Secondary Velocity Decomposition

In what follows, vectors are denoted by an overbar, and unit vectors by a caret. The analysis is based on decomposition of the overall velocity vector field \bar{U} into a primary flow velocity \bar{U}_p and a secondary flow velocity \bar{U}_s . The overall or composite velocity is determined from the superposition

$$\bar{U} = \bar{U}_p + \bar{U}_s \quad (1)$$

The primary flow velocity is represented as

$$\bar{U}_p = U_p \hat{i}_p \quad (2)$$

where \hat{i}_p is a known primary flow direction determined, for example, from an a priori potential flow solution for the geometry under consideration. A streamwise coordinate direction from a body fitted coordinate system could be used as an approximation to this flow direction. The primary velocity \bar{U}_p is determined from solution of a primary flow momentum equation in which the streamwise pressure gradient term is assumed known. The secondary flow velocity \bar{U}_s is derived from scalar and vector surface potentials, denoted by ϕ and ψ , respectively. If \hat{i}_n denotes the unit vector normal to transverse coordinate surfaces, if ρ is density, and if ρ_0 is an arbitrary constant reference density, then \bar{U}_s is defined by

$$\bar{U}_s \equiv \nabla_s \phi + \frac{\rho_0}{\rho} \nabla x \hat{i}_n \psi + \bar{V}_s \quad (3)$$

where ∇_s is the surface gradient operator defined by

$$\nabla_s \equiv \nabla - \hat{i}_n (\hat{i}_n \cdot \nabla) \quad (4)$$

and where \bar{V}_s is an arbitrary known vector field in the transverse coordinate surfaces. This vector field is usually set to zero; for the tip vortex flow analysis, however, \bar{V}_s is the transverse component of an inviscid flow

velocity computed for the geometry under consideration. This choice of \bar{V}_s facilitates the formulation of the boundary conditions, as will be seen in Section 2.11. It follows that since $\hat{i}_n \cdot \bar{U}_s = 0$, \bar{U}_s lies entirely within transverse coordinate surfaces. Equation (3) is a general form permitting both rotational and irrotational secondary flows and will lead to governing equations which may be solved as an initial-boundary value problem. The overall velocity decomposition (1) can be written as

$$\bar{U} = U_p \hat{i}_p + \nabla_s \phi + \frac{\rho_0}{\rho} \nabla x \hat{i}_n \psi + \bar{V}_s \quad (5)$$

2.2 Surface Potential Equations

Equations relating ϕ and ψ with U_p , ρ , and the secondary vorticity component Ω_n , can be derived using Eq. (5) as follows: From continuity,

$$\begin{aligned} \nabla \cdot \rho \bar{U} = 0 &= \nabla \cdot \rho U_p \hat{i}_p + \nabla \cdot \rho \nabla_s \phi \\ &+ \nabla \cdot \rho \nabla_s + \rho_0 \nabla \cdot \nabla x \hat{i}_n \psi \end{aligned} \quad (6)$$

and from the definition of the vorticity based on the secondary flow within the transverse surfaces, Ω_n ,

$$\begin{aligned} \hat{i}_n \cdot \nabla x \bar{U} \equiv \Omega_n &= \hat{i}_n \cdot \nabla x U_p \hat{i}_p + \hat{i}_n \cdot \nabla x \frac{\rho_0}{\rho} \nabla x \hat{i}_n \psi \\ &+ \hat{i}_n \cdot \nabla x \nabla_s + \hat{i}_n \cdot \nabla x \nabla_s \phi \end{aligned} \quad (7)$$

Since the last term in each of Eqs. (6) and (7) is zero by vector identity, Eqs. (6) and (7) can be written as

$$\nabla \cdot \rho \nabla_s \phi = -\nabla \cdot \rho U_p \hat{i}_p - \nabla \cdot \rho \bar{V}_s \quad (8)$$

and

$$\hat{i}_n \cdot \nabla x \frac{\rho_0}{\rho} \nabla x \hat{i}_n \psi = \Omega_n - \hat{i}_n \cdot \nabla x U_p \hat{i}_p - \hat{i}_n \cdot \nabla x \bar{V}_s \quad (9)$$

Note that the term $\hat{i}_n \cdot \nabla \times U_p \hat{i}_p$ in Eq. (9) is identically zero in a coordinate system for which \hat{i}_n and \hat{i}_p have the same direction, and would be small if \hat{i}_n and \hat{i}_p are approximately aligned. The term $\hat{i}_n \cdot \nabla \times \bar{V}_s$ is zero if \bar{V}_s comes from a potential flow solution. In any event, given a knowledge of \bar{U}_p , Ω_n , and ρ , the surface potentials ϕ and ψ can be determined by a two-dimensional elliptic calculation in transverse coordinate surfaces at each streamwise location. In turn, \bar{U}_s can be computed from Eq. (3), and the composite velocity U will satisfy continuity. Equations for U_p and Ω_n are obtained from the equations governing momentum and vorticity, respectively.

2.3 Streamwise Momentum

The streamwise momentum equation is given by

$$\hat{i}_p \cdot [(\rho \bar{U} \cdot \nabla) \bar{U} + \nabla p] = \hat{i}_p \cdot \rho \bar{F} + \hat{i}_p \cdot \rho \bar{R} \quad (10)$$

Here, p is the pressure, $\rho \bar{F}$ is the force due to viscous stress, and $\rho \bar{R}$ is the additional force due to a rotating coordinate system:

$$\bar{R} = -2\bar{\omega} \times \bar{U} - \bar{\omega} \times (\bar{\omega} \times \bar{r})$$

where $\bar{\omega}$ is the angular velocity of the coordinate system and \bar{r} is the radius vector from the rotation axis. Terms in \bar{F} representing streamwise diffusion are neglected. The pressure term in the streamwise momentum equation (10) can be taken from a simpler analysis such as a potential flow analysis.

2.4 Secondary Vorticity

The equation governing Ω_n is obtained by cross differentiating each of the transverse momentum equations:

$$\begin{aligned} \hat{i}_1 \cdot [(\rho \bar{U} \cdot \nabla) \bar{U} + \nabla p - \rho \bar{F} - \rho \bar{R}] &= 0 \\ \hat{i}_2 \cdot [(\rho \bar{U} \cdot \nabla) \bar{U} + \nabla p - \rho \bar{F} - \rho \bar{R}] &= 0 \end{aligned} \quad (11)$$

where \hat{i}_1 and \hat{i}_2 are two orthonormal vectors in the transverse coordinate surface. Eliminating the pressure in the two equations results in a single equation for the transport of the vorticity normal to the transverse surface. This equation has the form

$$\rho \bar{U} \cdot \nabla \bar{\Omega}_n - \bar{\Omega} \cdot \nabla \rho U_n = G_n + C + \hat{i}_n \cdot (\nabla \times \rho \bar{R}) \quad (12)$$

where $\bar{\Omega} = \nabla \times \bar{U}$ is the vorticity vector, G_n is the normal component of

$$\bar{G} = \nabla \times \rho \bar{F} \quad (13)$$

and C is a collection of curvature terms arising from changes in orientation of the transverse surfaces as a function of the streamwise coordinate.

2.5 Pressure Equation

While the above procedure results in a set of equations which can be solved by forward marching, the surface pressures which are due to the pressure field imposed upon the flow are the potential flow pressures. Since the actual surface pressures are often of primary interest, a new estimate of the actual surface pressure which includes viscous and secondary flow effects can be computed from the resulting velocity field in the following manner. The momentum equations (11) in the transverse surfaces represent components of the momentum vector in the transverse surfaces:

$$\begin{aligned} & \hat{i}_1 (\hat{i}_1 \cdot [(\rho \bar{U} \cdot \nabla) \bar{U} + \nabla p - \rho \bar{F} - \rho \bar{R}]) + \\ & \hat{i}_2 (\hat{i}_2 \cdot [(\rho \bar{U} \cdot \nabla) \bar{U} + \nabla p - \rho \bar{F} - \rho \bar{R}]) \end{aligned} \quad (14)$$

The divergence of this vector can be written as a Poisson equation for the pressure p at each transverse surface:

$$\begin{aligned} \nabla_s^2 p = \nabla_s^2 (p_I + p_C) = & - \frac{\partial}{\partial x_1} (\hat{i}_1 \cdot [(\rho \bar{U} \cdot \nabla) \bar{U} - \rho \bar{F} - \rho \bar{R}]) \\ & - \frac{\partial}{\partial x_2} (\hat{i}_2 \cdot [(\rho \bar{U} \cdot \nabla) \bar{U} - \rho \bar{F} - \rho \bar{R}]) \end{aligned} \quad (15)$$

where p_I is the imposed pressure, p_c is a viscous correction to the pressure field and x_1 and x_2 are coordinates in the \hat{i}_1 and \hat{i}_2 directions, respectively. Equation (15) can be solved for the pressure correction p_c at each computational station using Neuman boundary conditions derived from Eq. (14). The use of Neuman boundary conditions requires an additional parameter which is only a function of the normal direction, $p_v(x_3)$, in order to set the level of the pressure field. For external flows, $p_v(x_3)$ is set to match the imposed pressure at an appropriate far field location, obtained, for example, from an a priori potential flow solution for the geometry under consideration.

In the actual numerical solution procedure, the streamwise (x_3 -) derivatives of the scalar potential (ϕ -) velocities are not always smooth, and their effect on the pressure field computed from Eq. (15) can be detrimental. Therefore, the terms $\frac{\partial}{\partial x_3} (\nabla_s \phi)$ that are part of the $(\rho \bar{U} \cdot \nabla) \bar{U}$ terms in Eq. 15 are neglected. This approximation leads to improved accuracy of the computed viscous pressure field, as verified by comparison with experimental data.

2.6 The Gas Law Equation

For incompressible flow, density is a constant value and the Eqs. (10), (12), (8), (9), and (15) form the required governing set. For compressible flow, an additional equation relating the density to the other flow variables is required. Such an equation is obtained from the perfect gas law

$$p = \rho RT \quad (16)$$

where R is the gas constant. Assuming constant total temperature T_0 , Eq. (16) can be written as

$$p = \rho R(T_0 - \frac{\bar{U} \cdot \bar{U}}{2C_p}) \quad (17)$$

where C_p is the heat capacity of the gas at constant pressure. Equation (17) relates density, pressure, and velocity. If the total temperature assumption is inadequate, an energy equation can be added to the system and solved coupled with the streamwise momentum equation.

2.7 Turbulence Model

In the high Reynolds number flows addressed in this report, it is necessary to specify a turbulence model. At present, a simple mixing length type

model is used in the analysis. In internal flow applications of this analysis, quantitatively accurate flow simulations have been obtained with a mixing-length approach (Refs. 5, 7, 8). The mixing-length turbulence model employed here computes an eddy viscosity μ_T from the expression (Ref. 9):

$$\frac{\mu_T}{\text{Re}} = \rho \ell^2 (\bar{\bar{e}} : \bar{\bar{e}})^{1/2} \quad (18)$$

where Re is the Reynolds number, $\bar{\bar{e}}$ is the mean flow rate of strain tensor

$$\bar{\bar{e}} = \frac{1}{2} [\nabla \bar{U} + (\nabla \bar{U})^T] \quad (19)$$

and ℓ is the mixing length determined from the empirical relationship of McDonald and Camarata (Ref. 10) for equilibrium turbulent boundary layers:

$$\ell(y) = 0.09 \delta_b \tanh\left[\frac{\kappa y}{0.09\delta_b}\right] D \quad (20)$$

Here, y is the distance from the wall, δ_b is the local boundary layer thickness, κ is the Von Karman constant (taken as 0.43), and D is a sublayer damping factor

$$D = P^{1/2} \left\{ \frac{y^+ - \bar{y}^+}{\bar{\sigma}} \right\} \quad (21)$$

where P is the normal probability function, $\bar{\sigma} = 8$, $\bar{y}^+ = 23$, and

$$y^+ = y \frac{(\tau/\rho)^{1/2}}{(\nu/\rho)} \quad (22)$$

with τ being the local shear stress and ν the viscosity of the fluid.

2.8 Governing System of Equations

A complete system of five coupled equations governing U_p , Ω_n , ϕ , ψ , and p is given by Eqs. (10), (12), (8), (9), and (15). For compressible flows, Eq. (17) is added for ρ . The ancillary relations (5) and (18)-(22) are given for the composite velocity and the eddy viscosity. In Ref. 6 the governing equations are given in general orthogonal coordinates, and in Ref. 7 in nonorthogonal coordinates.

2.9 Numerical Method

Since techniques for obtaining the basic potential flow solution are well known and numerous, they need not be enumerated or discussed here. Instead, the present development concentrates on describing the numerical method used to solve the system of governing equations. Streamwise derivative terms in the governing equations have a form such as $U_p \partial(\) / \partial x_3$, and because the streamwise velocity U_p is very small in the viscous dominated region near no-slip walls, it is essential to use implicit algorithms which are not subject to stringent stability restrictions unrelated to accuracy requirements. Although it is possible to devise algorithms for the solution of the governing equations as a fully coupled implicit system, such algorithms would require considerable iteration for the system of equations treated here, and this would detract from the overall efficiency. The present method is semi-implicit and seeks to reduce the amount of iteration required and yet avoid the more severe stability restrictions of explicit algorithms. The method partitions the system of governing equations into subsystems which govern the primary flow, the secondary flow, and the turbulence model. The primary-flow subset of equations contains the streamwise momentum equation (plus an energy equation, if needed). The secondary-flow subset of equations contains the secondary vorticity equation and the scalar and vector potential equations. These subsystems are decoupled using an ad hoc linearization in which secondary velocity components and turbulent viscosity are lagged, and are solved sequentially during each streamwise step.

2.10 Summary of Algorithm

The governing equations are replaced by finite-difference approximations. Three-point central difference formulas are used for all transverse spatial derivatives. Analytical coordinate transformations are employed as a means of introducing a nonuniform grid in each transverse coordinate direction, as appropriate, to concentrate grid points in the wall boundary layer regions. Second-order accuracy for the transverse directions is rigorously maintained. Two-point backward difference approximations are used for streamwise derivatives, although this is not essential.

To solve the primary flow subsystem of viscous equations, a scalar ADI scheme is used for the momentum equation.

Given the solution for the primary flow, the secondary flow subsystem can be solved. First, the scalar potential equation (continuity) is solved using a scalar iterative ADI scheme. Next, the secondary vorticity and vector potential equations are written as a fully implicit coupled system and solved using an iterative linearized block implicit (LBI) scheme (cf. Briley and McDonald, Ref. 11). In selecting boundary conditions for the secondary flow subsystem, care must be taken to ensure that the final secondary velocity satisfies the no-slip condition accurately. In the scalar potential equation the normal derivative of ϕ is set equal to minus the normal component of \bar{V}_s . This boundary condition corresponds to zero normal velocity. It is not possible to simultaneously specify the tangential velocity, however, and thus the \bar{V}_s - and ϕ -contributions to the secondary velocity will have a nonzero tangential (slip) component, denoted V_t , at solid boundaries. In the coupled vorticity and vector-potential equations, both the normal and the tangential velocity component can be specified as boundary conditions, since these equations are solved as a coupled system. By choosing (a) zero normal velocity, and (b) minus V_t as the ψ -contribution to the tangential velocity, the slip velocity V_t arising from the ϕ calculation is cancelled, and the composite secondary flow velocity including \bar{V}_s , ϕ , and ψ contributions will satisfy the no-slip condition exactly.

A summary of the overall algorithm used to advance the solution a single axial step follows. It is assumed that the solution is known at the n -level x_3^n (the n^{th} transverse plane) and is desired at x_3^{n+1} .

- (1) The imposed streamwise pressure gradient distribution and the vector field \bar{V}_s are determined from an inviscid potential flow.
- (2) The momentum equation is solved to determine U_p^{n+1} . For compressible flows, ρ^{n+1} is obtained from Eq. (17).
- (3) Using values now available for ρ^{n+1} and U_p^{n+1} , the scalar potential equation (8) is solved using an iterative scalar ADI scheme, to obtain ϕ^{n+1} . This ensures that the continuity equation is satisfied.

- (4) The equations for vorticity (12) and vector potential (9) form a coupled system for Ω_n^{n+1} and ψ^{n+1} which is solved as a coupled system using an iterative LBI scheme.
- (5) Values for the two components of the transverse velocity vector \bar{U}_s are computed from Eq. (3).
- (6) Using the computed velocity field, the transverse pressure field is computed from Eq. (13) by an iterative scalar ADI scheme.
- (7) The eddy viscosity is updated using Eqs. (18)-(22).

2.11 Boundary Conditions for the Tip Vortex Flow Computations

Figure 2 shows a perspective view of a straight blade with NACA 0012 airfoil section and a rounded tip. For this case, the transverse coordinate surfaces were taken normal to the chord line of an airfoil section. Figure 3 shown a cross-section of the blade tip and the computational grid at a typical streamwise station. A computational grid that wraps around the tip was chosen to provide adequate resolution of the tip region and a smooth grid distribution.

The cross-sectional computational coordinate system, shown in Fig. 3, has four boundaries where boundary conditions for the governing equations must be specified. Inboard are boundaries AB and CD, the blade surface is boundary BC, and the far field is boundary AD. Boundary conditions must be specified for the streamwise velocity in the streamwise momentum equation, for the scalar potential in the scalar potential equation, and for the vector potential and streamwise vorticity in the coupled vector potential - streamwise vorticity equations. The conditions that were specified for the tip vortex flow computations are considered in this section.

The flow at the inboard boundaries AB and CD was assumed to be quasi two-dimensional (no spanwise variation). The streamwise velocity was extrapolated from the interior flow field, and the normal gradient of the scalar potential was set to zero. The vector field \bar{V}_s was assumed to be derived from an inviscid flow field for the geometry under consideration. Neglecting spanwise variations, the coupled vector potential - vorticity

equations were solved as two-point boundary value problems along the inboard boundaries. Boundary conditions for these problems were the no-slip and no through-flow velocity conditions on the blade surface (at B and C of Fig. 3), and the inviscid spanwise velocity and zero streamwise vorticity at the outer boundary (at A and D of Fig. 3). Since the inviscid spanwise velocity is included in \bar{V}_s , these boundary conditions pose no special problems. The solutions to the boundary value problems were used as function boundary conditions on the vector potential and streamwise vorticity for the interior tip flow field. The inboard boundary treatment outlined above is similar to the one proposed in Ref. 4. It allows through-flow through the inboard boundaries, and permits these boundaries to be placed closer to the tip.

The boundary condition along boundary BC, the blade, was the no-slip condition on a solid surface. To satisfy this condition, the normal gradient of the scalar potential (the normal velocity) was set to cancel the normal component of \bar{V}_s . In the coupled vector potential and vorticity equations the normal component of the rotational velocity was set to zero, and the tangential component was set equal and opposite to the tangential component of the velocity generated by the scalar potential and the vector field \bar{V}_s . These conditions allowed an implicit specification of the vector potential and the vorticity on the no-slip boundary (as discussed in Section 2.10). The resultant secondary velocity field satisfies the no-slip conditions on the boundary. The streamwise velocity was also set to zero at the solid boundary.

Far field conditions were specified on boundary AD. The streamwise velocity was extrapolated from the interior flow field. The scalar potential was set to a constant, so that the tangential component of the ϕ -contribution to the irrotational velocity was zero. This condition allowed outflow through the boundary due to the displacement effect of the boundary layers on the blade. The vector potential was varied linearly between its values at A and D as obtained from the inboard boundary conditions described above, and the streamwise vorticity was set to zero. Because \bar{V}_s was assumed to be an inviscid cross-flow velocity field, the angle of incidence of the flow and the global effect of the geometry were included automatically.

It should be noted that the far field boundary condition was the main reason for including \bar{V}_s in the secondary flow velocity decomposition. In previous tip vortex calculations (Refs. 2-4), the effect of the angle of incidence of the flow had been included in the boundary condition on the vector

potential, and the effect of the global geometry had not been taken into account. This effect is important because of the proximity of the outer boundary to the tip. As a result, the tip vortex in those previous calculations was driven too strongly by the outer boundary conditions. The present boundary conditions avoid this problem, and permit the outer boundary to be relatively close to the blade surface.

3. RESULTS

To quantitatively assess the capability of the forward-marching analysis to compute the tip vortex generation process, results of the computations are compared with experimental data for tip vortex generation. Such data are not widely available, but do exist (e.g. Gray et al. (Ref. 1), Francis and Kennedy (Ref. 12), and Chigier and Corsiglia (Ref. 13)). In the present study, two flow cases for tip vortex generation on a model helicopter blade in hover are studied, for which data at pitch angles of 6.18° and 11.4° are given by Gray et al. (Ref. 1). A third case addresses the computation of flow downstream of the blade. The blade is straight, with an NACA 0012 untwisted airfoil section and a rounded tip (cf. Fig. 2). The important geometric and flow parameters are:

Tip radius/blade chord	= 4.8
Pitch angle	= 6.18° and 11.4°
Reynolds number (based on tip velocity and chord)	= 736000
Mach number (based on tip velocity)	= 0.25

The experimental data consist of static pressure measurements on the blade surface in the tip region. The calculations were performed in two steps. First an inviscid (potential) flow field was generated. Then the viscous flow analysis was performed using the streamwise pressure gradient and cross-plane velocity vector field obtained from the inviscid flow field.

3.1 The Inviscid Flow Calculations

The inviscid flow field was generated using a panel method code developed by Hess (Ref. 14). The calculations were done for a non-rotating blade. Since the region of interest was the tip region, the panel code was applied to a

symmetric "wing" with a half-span of $3c$ (where c denotes the blade chord), at angles of incidence of 6.18° and 11.4° . Increasing the wing span did not appreciably alter the inviscid flow field near the tip. 1280 panels were used on the lifting part of the wing (with a higher panel density near the leading edge and the tip), 40 panels on the non-lifting tip-body, and 320 panels in the wake. Figures 4 and 5 show the resulting chordwise and spanwise pressure distributions on the blade, as obtained from the velocities computed at the panel centers. In these figures, x is a chordwise coordinate ($x/c = 0$ at the leading edge and $x/c = 1$ at the trailing edge), while y is a spanwise coordinate ($y/c = 0$ at the symmetry plane and $y/c = 3$ at the tip). Two problems arose in the computation of the inviscid field:

- (i) Since the panel method used is a first-order method, the inviscid velocity field is not smooth near the blade surface.
- (ii) The inviscid flow around the tip is nonunique, because it is not known a priori where the wake leaves the tip body. Since no empirical information is to be used in the calculations, the ambiguity cannot be resolved. For the present calculation, the tip half-body of revolution is treated as a nonlifting body. As a consequence, the transverse inviscid velocities around the tip are large, especially in the vicinity of the trailing edge, leading to unrealistic pressures.

The above problems imply that the computed inviscid field will not be accurate close to the blade surface. A short distance away from the surface, however, the inviscid field is well-behaved. And since the inviscid field is used only to generate an approximate streamwise pressure gradient and an outer boundary cross-plane velocity vector field for the viscous flow analysis, it is acceptable to ignore the inaccurate part of the inviscid field, and to use interpolation to regenerate a smooth field near the blade surface. Figure 6 shows contours of the inviscid pressure field so obtained on the suction side of the blade tip surface. The left-most part of this figure shows the location of both the region on the suction surface on which the computational results are presented and the innermost rectangle in which experimental data are available (data taken closer to the leading edge are not included in the present data comparison). The latter region is also indicated by a dashed

rectangle in the middle part of Fig. 6, which shows contours of the computed inviscid pressure distribution. The comparison with the experimental data from Gray et al. (Ref. 1) shows clearly that the inviscid field does not contain a tip vortex, and that the viscous pressure relief near the trailing edge of the blade is missing.

3.2 The Viscous Flow Calculation for 6.18° Incidence

The viscous flow calculation was performed in the tip region of the blade described above. As mentioned in Section 2.11, the marching direction coincided with the chordwise direction. Figure 2 shows a perspective view of the blade geometry near the tip, and Fig. 3 shows the cross-section of the blade tip and the computational grid at a typical streamwise station. This latter figure also shows the extent of the computational domain: the inboard boundaries (AB and CD in Fig. 3) were located at a distance $0.4 c$ from the tip, while the outer boundary (AD in Fig. 3) was located a distance $0.3 c$ away from the blade surface.

A computational grid of 120 streamwise stations and a 47×40 cross-plane grid was used (totaling 225,600 grid points). Grid points were clustered in regions of high flow gradients, such as near the blade surface and in the tip region (cf. Fig. 3). The computation was started at a distance of $0.15 c$ from the leading edge of the blade with an assumed initial boundary layer thickness of $0.003 c$. Given this boundary layer thickness, an initial streamwise velocity distribution was constructed using a standard boundary layer profile. The marching scheme was then applied to the initial station without updating the streamwise velocity, to obtain a consistent set of initial distributions of the dependent variables, from which the actual marching procedure was started. The last station was at $0.06 c$ from the trailing edge of the blade. The computer run time for this particular tip vortex flow field computation was about 7 minutes on a CRAY-1 computer system with a partially vectorized code. Results of the computation, which was performed under the operating conditions specified above, but for a non-rotating blade, are shown in Figs. 7-11.

Figure 7 shows the development of the tip vortex computed by the code in terms of streamwise velocity contours. Computations from four streamwise stations ($x/c = 0.57, 0.74, 0.84$ and 0.94 , where x is the distance from the

leading edge) were chosen to display the development of the tip vortex in the tip region, which extends $0.11 c$ in the spanwise direction. The basic flow mechanisms that result in the generation of the tip vortex have been described by Govindan et al. (Ref. 3). These mechanisms are the transport of low momentum fluid from the pressure side boundary layer to the suction side by the transverse velocity, the accumulation of this low momentum fluid on the suction side of the tip region, and the roll-up of this accumulated fluid into the tip vortex.

That, indeed, the flow in the tip region rolls up into the tip vortex is clearly visualized by the vector plots of the transverse velocity field in the tip region (Fig. 8). The large transverse velocities (up to about 80% of the free stream velocity at $x/c = 0.94$) around the tip that convect the low momentum fluid from the pressure side to the suction side are also seen. Figure 9 shows a vector plot of the cross-plane velocities at $x/c = 0.94$ in the full computational domain. The flow through the inboard boundaries (AB and CD in Fig. 3) is clearly visible, indicating the effectiveness of the inboard boundary conditions described in Section 2.11. Contour plots of the computed transverse pressure fields are shown in Fig. 10. The low pressure region near the tip can be seen clearly, as can the development of a low pressure region associated with the tip vortex. This low pressure region would determine the cavitation characteristics of the tip flow field.

At this point, it should be noted that the tip vortex generation process has been calculated from a set of three-dimensional, viscous flow equations which have a no-slip condition at the blade surface. The vortex generation and roll-up is a result of the secondary flow separation and can be analyzed from a consideration of the basic physical phenomena without resorting to empirical models.

3.3 Data Comparison for 6.18° Incidence

Figure 11 shows a streamwise contour plot of the computed pressure field on the suction side of the blade. This pressure field is compared with the inviscid pressure field discussed in Section 3.1 and with the experimental data of Gray et al. (Ref. 1). The following observations can be made:

- (i) The computed viscous flow field is qualitatively correct.
- (ii) There is quantitative agreement with the experimental data in the inboard pressure distribution, the spanwise variation of the pressure near the inboard boundary, and the pressure variation across the tip vortex, although this vortex forms too far aft on the blade.

These observations are in sharp contrast with the observations made for the inviscid flow field (see Section 3.1). Clearly, the forward-marching analysis is capable of predicting not only the qualitative features of the tip vortex generation process, but also the quantitative features. Several aspects of the present analysis, however, need refinement:

- (a) Initial conditions: In essence, the initial conditions are obtained by adding a boundary layer profile to the inviscid velocity field at the first station (see Section 3.2). The spanwise variation of the initial boundary layer thickness has not been accounted for.
- (b) Grid resolution: To capture the turbulent boundary layer (which is very thin, especially on the pressure side of the blade and on the tip), a very fine mesh is needed near the blade surface. When the tip vortex forms, a fine grid is also required in the vortex itself. Although the present grid is relatively fine (cf. Fig. 3), it is still somewhat of a compromise between the above requirements. A solution-adaptive grid generation technique may be required to accommodate a sufficient number of grid points in the boundary layer (whose thickness varies both in chordwise and in spanwise direction) and in the tip vortex without a substantial increase in the total number of grid points.
- (c) Turbulence model: As described in Section 2.7, the turbulence model used is an algebraic eddy viscosity model based on an appropriate flow field length scale. Although the turbulence model determines the state of the boundary layer being swept around the tip to create the tip vortex, this flow is wall flow where the length scale is known to be proportional to distance from the wall. Once the tip vortex separates from the wall, the major effect may be secondary flow rather than

turbulent effects per se. Therefore, the simple turbulence model may be appropriate. A more complex model could, however, be included in the current computer code.

- (d) Streamwise pressure gradient: As mentioned in Section 3.1, the present inviscid flow field lacks smoothness and accuracy in the vicinity of the blade surface. As a consequence, the streamwise inviscid pressure gradient used as input to the viscous flow analysis is not as good as it could be. The use of a higher-order panel method and a refined tip treatment may improve the situation.
- (e) Rotation: The calculations were performed for a non-rotating blade. Previous experience (Ref. 3) indicates that the effect of rotation on the tip vortex generation is small (though not unnoticeable). The main problems are the estimate of the streamwise inviscid pressure gradient and the far-field boundary conditions.

Preliminary studies have indicated that the above-mentioned aspects of the analysis do not have a strong effect on the computation of the tip vortex generation process, but may be important to improve the quantitative agreement with the experimental data.

3.4 Computed Results for 11.4° Incidence

In addition to data for a blade pitch angle of 6.18°, Gray et al. (Ref. 1) provides experimental data for a blade pitch angle of 11.4°. Therefore, a second calculation was done, similar to the first one, but for the (non-rotating) blade at an angle of incidence of $\alpha = 11.4^\circ$ instead of $\alpha = 6.18^\circ$. The computation was halted at a distance of 0.11 c from the trailing edge of the blade, because streamwise separation was encountered further downstream. Results of this computation are shown in Figs. 12-15.

Figure 12 shows a streamwise contour plot of the computed viscous pressure field on the suction side of the blade, compared with the (computed) inviscid pressure distribution and the experimental data of Gray et al. (Ref. 1). The

agreement of the computed results with the experimental data is similar to the one discussed in Section 3.3 for the 6.18° angle of incidence case. A comparison of Figs. 11 and 12 shows that the tip vortex is much stronger than in the previous case, which is also illustrated in Figs. 13-15. Figure 13 shows a vector plot of the transverse velocity field, while Figs. 14 and 15 show contour plots of the streamwise velocity, the inviscid pressure coefficient, and the viscous pressure coefficient in the tip region at the streamwise station $x/c = 0.89$. The low pressure region that is associated with the tip vortex is clearly visible, and a comparison with the inviscid pressure distribution once again shows that the inviscid field does not contain a tip vortex.

The above results reinforce the conclusions drawn in Section 3.3, and build up confidence in the results obtained from the forward marching analysis.

3.5 Additional Results Downstream of the Trailing Edge

A natural continuation of the calculations discussed in the previous sections would be to continue the computation downstream of the blade trailing edge. A general capability would allow for computation of the flow downstream of swept trailing edges, and data is available for this type of configuration. Although the capability for treating swept trailing edges was under investigation in a related program, this capability was not completed for use in the present study. Consequently, the present study considers a test case having an unswept trailing edge. To demonstrate the capability of the forward-marching procedure to compute the development of the tip vortex downstream of an unswept trailing edge, a calculation was performed for the blade described in Section 3.2, at an angle of incidence of 6.18° . The inviscid flow field was not used in this calculation; the streamwise pressure gradient was set to zero, and the far field boundary conditions were included in the vector potential ψ . A simple turbulence model was used in the region downstream of the trailing edge. Fig. 16 shows the results of this calculation.

Streamwise velocity contour plots, shown at three streamwise stations ($x/c = 1.0, 1.7$, and 2.5), illustrate the dissipation of the vortex.

It should be emphasized that these results are of a qualitative nature. To obtain results that can be compared with experimental data, it is necessary to:

- (i) Include the inviscid streamwise pressure gradient in the streamwise momentum equation,
- (ii) Include the effect of the inviscid transverse plane velocity components in the far field boundary conditions (by including these velocity components in the transverse plane velocity decomposition),
- (iii) Choose an appropriate turbulence model.

The first two aspects require additional work on the interface between the inviscid flow solver and the forward marching scheme in the region downstream of the blade trailing edge. As far as the third aspect is concerned, experience with the use of different turbulence models has shown that although the turbulence model does not greatly affect the formulation of the tip vortex, it does play an important role in the speed with which the tip vortex dissipates once it has formed and has separated from the wall. Therefore, a proper turbulence model should be chosen for the region downstream of the blade trailing edge before a data comparison is performed.

4. CONCLUSIONS

Previous work (Refs. 2-4) has shown the feasibility of utilizing a three-dimensional forward marching analysis for the tip vortex generation problem. The present analysis has clearly demonstrated the capability of the forward-marching procedure to compute the quantitative features of the tip vortex flow field without the use of empirical information. Comparison with experimental data has shown good agreement. It is evident that the procedure can compute the low pressure region in the flow associated with the tip vortex, and can help in identifying regions of the flow field that may be susceptible to cavitation.

The computations are economical compared to computing solutions of the full Navier-Stokes equations for tip vortex flow fields, which makes the procedure suitable for the design and analysis of ship propeller blades.

Future efforts are aimed at refining the current analysis, and at building a high level of confidence in the results obtained from the analysis, by making additional quantitative comparisons of the computations of the tip flow field with experimental data.

ACKNOWLEDGEMENT

The authors would like to thank Dr. T.M. Tsai for his calculation of the tip vortex development downstream of the blade trailing edge, discussed in Section 3.5 (cf. Fig. 16).

REFERENCES

1. Gray, R.B., McMahon, H.M., Shenoy, K.R., and Hammer, M.L., "Surface Pressure Measurements at Two Tips of a Model Helicopter Rotor in Hover", NASA CR-3281, 1980.
2. Shamroth, S.J. and Briley, W.R., "A Viscous Flow Analysis for the Tip Vortex Generation Problem", NASA CR-3184, 1979.
3. Govindan, T.R., Levy, R., and Shamroth, S.J., "Computation of the Tip Vortex Generation Process for Ship Propeller Blades", Fourth International Conference on Numerical Ship Hydrodynamics, Washington, D.C., 1985.
4. Lin, S.-J., Levy, R., Shamroth, S.J., and Govindan, T.R., "A Three-Dimensional Viscous Flow Analysis for the Helicopter Tip Vortex Generation Problem", NASA CR 3906, 1985.
5. Briley, W.R. and McDonald, H., "Analysis and Computation of Viscous Subsonic Primary and Secondary Flows", AIAA Paper 79-1453, 1979.
6. Kreskovsky, J.P., Briley, W.R., and McDonald, H., "Prediction of Laminar and Turbulent Primary and Secondary Flows in Strongly Curved Ducts", NASA CR-3388, 1981.
7. Levy, R., Briley, W.R., and McDonald, H., "Viscous Primary/Secondary Flow Analysis for Use with Nonorthogonal Coordinate Systems", AIAA Paper 83-0556, 1983.
8. Towne, C.E., "Computation of Viscous Flow in Curved Ducts and Comparison with Experimental Data", AIAA Paper 84-0531, 1984.
9. Beer, J.M. and Chigier, N.A., Combustion Aerodynamics, Wiley, New York, 1972.
10. McDonald, H. and Camarata, F.J., "An Extended Mixing Length Approach for Computing the Turbulent Boundary-Layer Development", Stanford Conference on Computation of Turbulent Boundary Layers, 1969.
11. Briley, W.R. and McDonald, H., "On the Structure and Use of Linearized Block Implicit Schemes", Journal of Computational Physics, Vol. 34, 1980, pp. 54-73.
12. Francis, M.S. and Kennedy, D.A., "Formation of a Trailing Vortex", Journal of Aircraft, Vol. 16, 1979, pp. 148-154.
13. Chigier, N.A. and Corsiglia, V.R., "Tip Vortices - Velocity Distributions", 27th Annual National V/STOL Forum, American Helicopter Society, Washington, DC, 1971.
14. Hess, J.L., "Calculation of Potential Flow about Arbitrary Three-Dimensional Lifting Bodies", Douglas Aircraft Company Report MDC J5679-01, Long Beach, 1972.

List of Figures

1. Tip region flow field
2. Perspective view of the blade tip
3. Transverse computational grid at $x/c = 0.74$
4. Chordwise inviscid pressure distributions at several spanwise stations
5. Spanwise inviscid pressure distributions at several chordwise stations
6. Comparison of the inviscid and the experimental pressure coefficient distribution on the suction side of the blade
7. Streamwise velocity distributions in the tip region at several streamwise stations (contour levels: 0.5, 0.6, ..., 0.9 times the free-stream velocity)
8. Vector plots of transverse velocities normalized by the free-stream velocity in the tip region at several streamwise stations
9. Vector plot of transverse velocities normalized by the free-stream velocity in the full domain at $x/c = 0.94$
10. Pressure coefficient distributions in the tip region at several streamwise stations (contour interval: -0.03)
11. Inviscid, viscous, and experimental pressure coefficient distributions on the suction side of the blade
12. Inviscid, viscous, and experimental pressure coefficient distributions on the suction side of the blade, for $\alpha = 11.4^\circ$
13. Vector plot of transverse velocities (normalized by the free-stream velocity) in the tip region at $x/c = 0.89$, for $\alpha = 11.4^\circ$
14. Streamwise velocity distribution in the tip region at $x/c = 0.89$, for $\alpha = 11.4^\circ$ (contour levels: 0.5, 0.6, ..., 0.9 times the free-stream velocity)
15. Pressure coefficient distributions in the tip region at $x/c = 0.89$, for $\alpha = 11.4^\circ$ (contour interval: -0.1)
 - (a) Inviscid pressure
 - (b) Viscous pressure
16. Streamwise velocity distributions at several streamwise stations downstream of the blade trailing edge

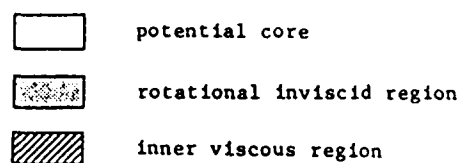
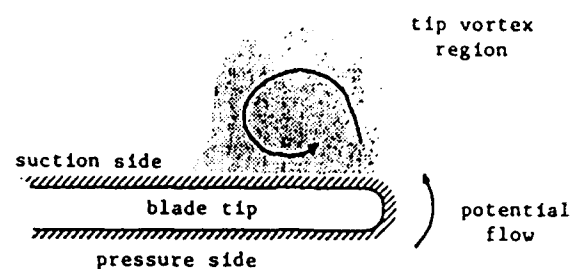


Fig. 1 Tip region flow field

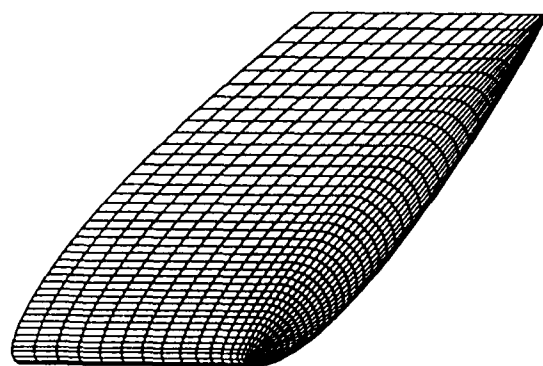


Fig. 2 Perspective view of the blade tip

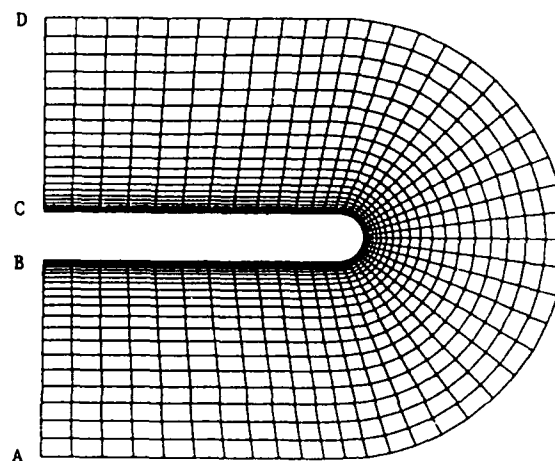


Fig. 3 Transverse computational grid at $x/c = 0.74$

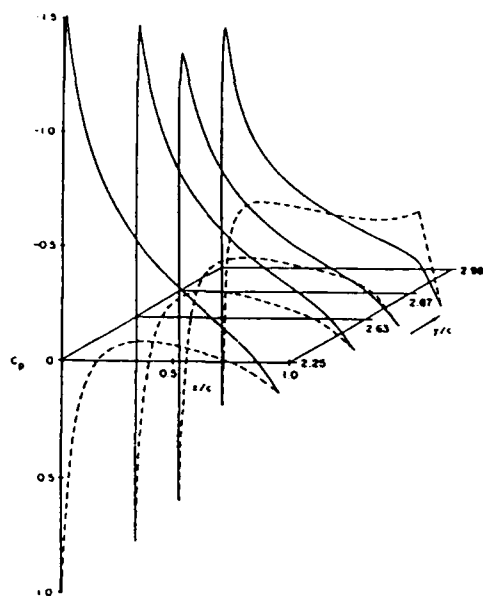


Fig. 4 Chordwise inviscid pressure distributions at several spanwise stations

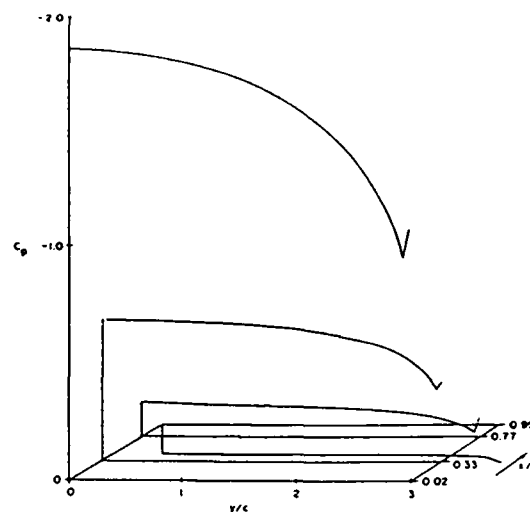


Fig. 5 Spanwise inviscid pressure distributions at several chordwise stations

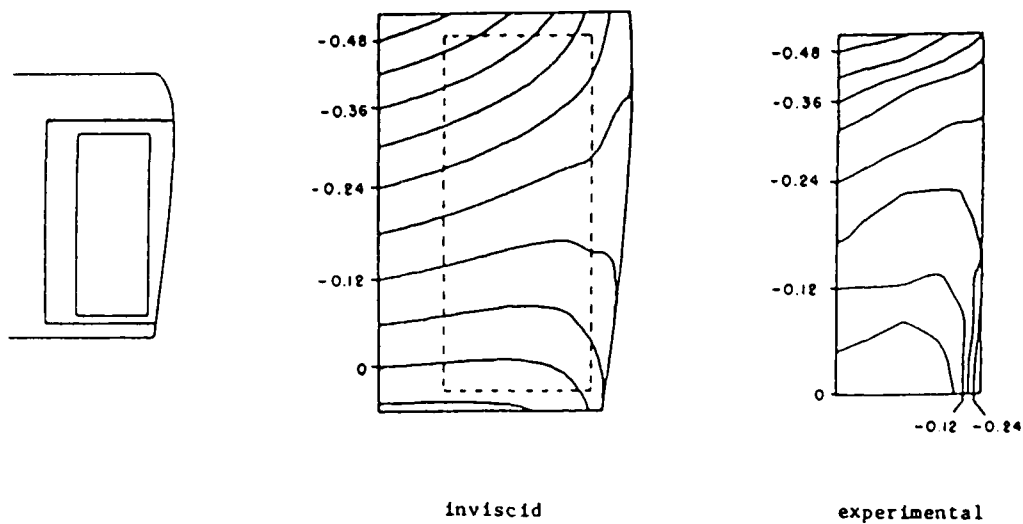
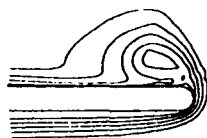
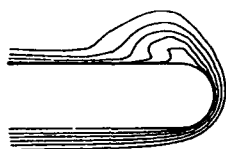


Fig. 6 Comparison of the inviscid and the experimental pressure coefficient distribution on the suction side of the blade

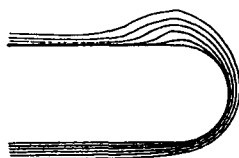
$x/c = 0.94$



$x/c = 0.84$



$x/c = 0.74$



$x/c = 0.57$

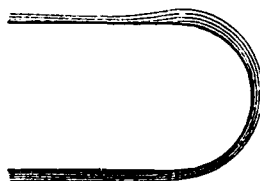
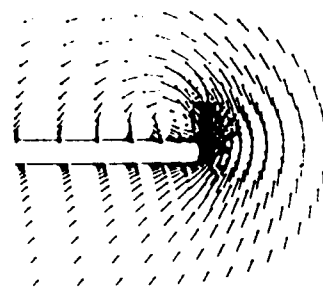
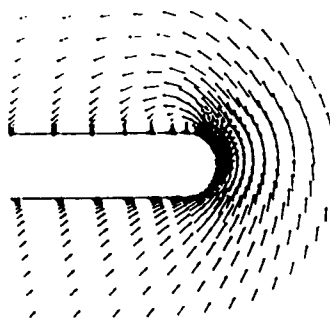


Fig. 7 Streamwise velocity distributions in the tip region at several streamwise stations (contour levels: 0.5, 0.6, ..., 0.9 times the free-stream velocity)

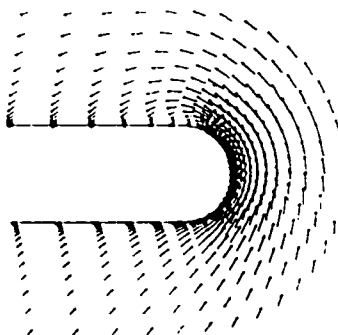
$x/c = 0.94$



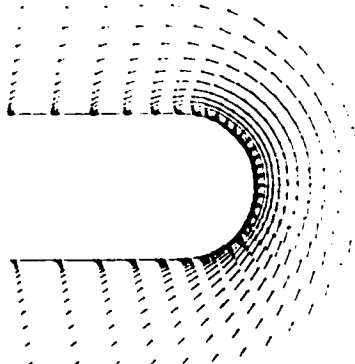
$x/c = 0.84$



$x/c = 0.74$



$x/c = 0.57$



0.5

Fig. 8 Vector plots of transverse velocities (normalized by the free-stream velocity) in the tip region at several streamwise stations

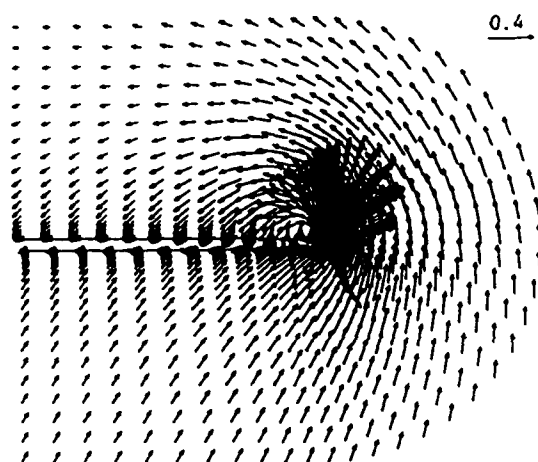


Fig. 9 Vector plot of transverse velocities (normalized by the free-stream velocity) in the full domain at $x/c = 0.94$

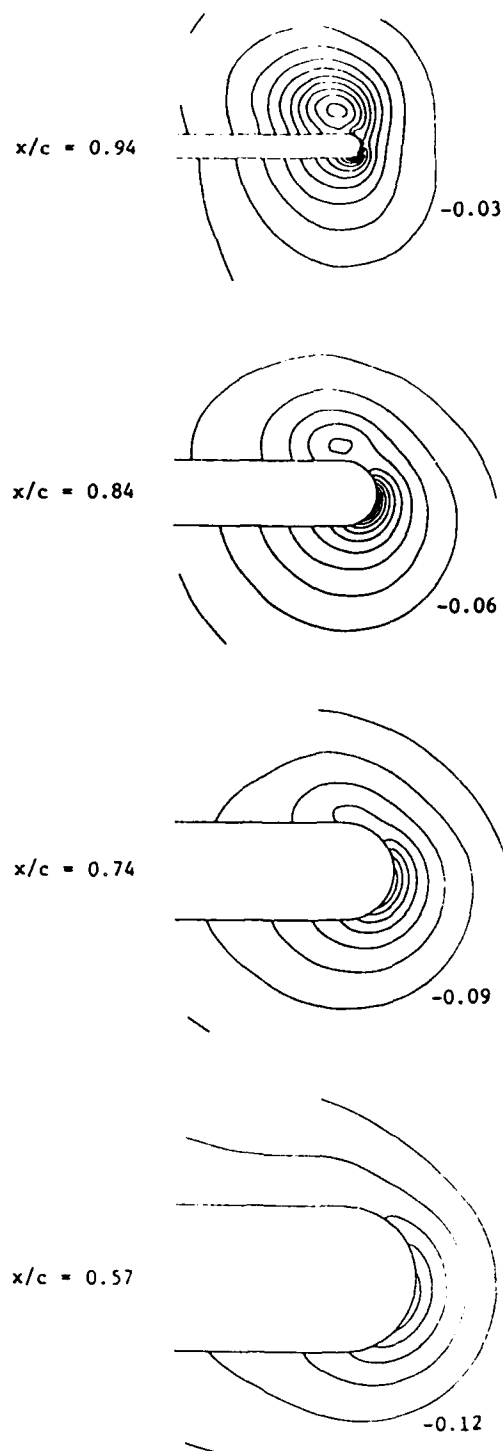


Fig. 10 Pressure coefficient distributions in the tip region at several streamwise stations (contour interval: -0.03)

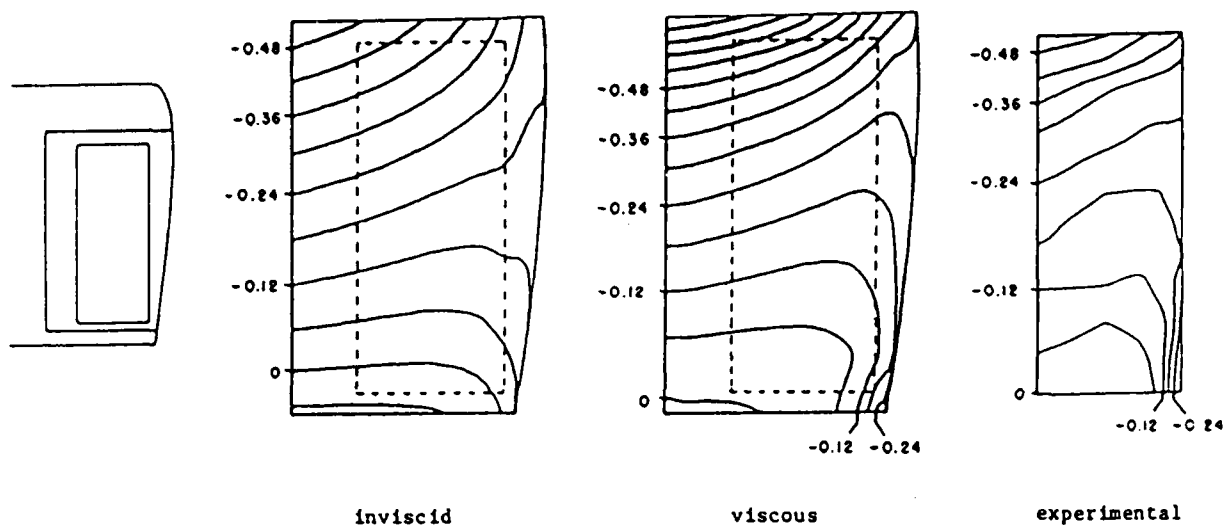


Fig. 11 Inviscid, viscous, and experimental pressure coefficient distributions on the suction side of the blade

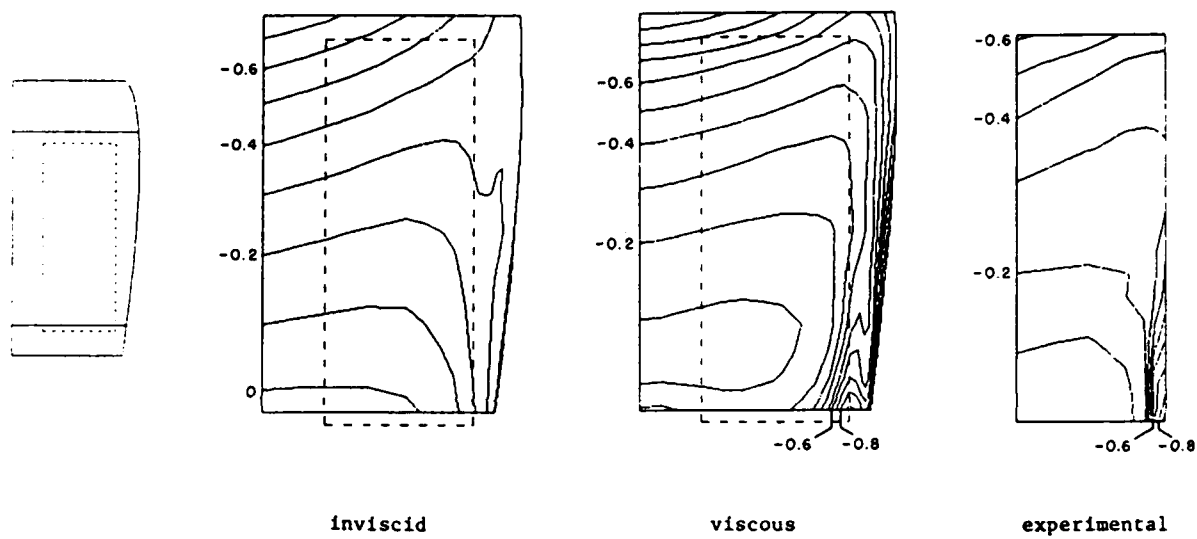


Fig. 12 Inviscid, viscous, and experimental pressure coefficient distributions on the suction side of the blade, for $\alpha = 11.4^\circ$

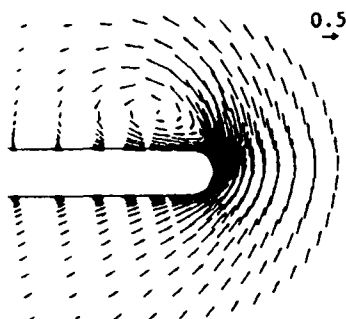


Fig. 13 Vector plot of transverse velocities (normalized by the free-stream velocity) in the tip region at $x/c = 0.89$, for $\alpha = 11.4^\circ$

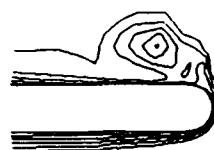
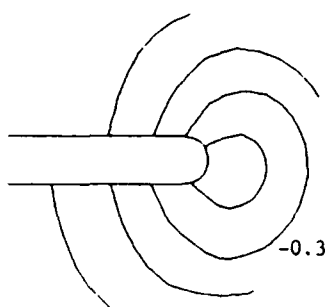
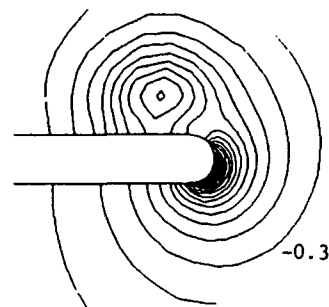


Fig. 14 Streamwise velocity distribution in the tip region at $x/c = 0.89$, for $\alpha = 11.4^\circ$ (contour levels: 0.5, 0.6, ..., 0.9 times the free-stream velocity)



(a) inviscid



(b) viscous

Fig. 15 Pressure coefficient distributions in the tip region at $x/c = 0.89$, for $\alpha = 11.4^\circ$ (contour interval: -0.1)

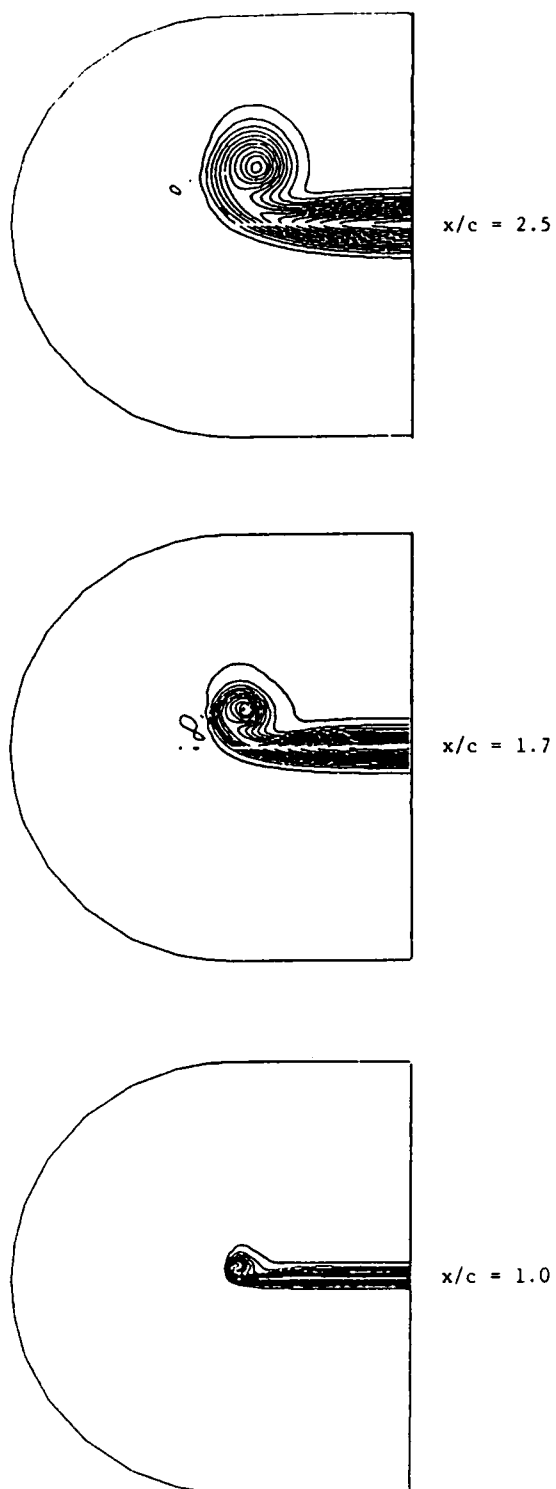


Fig. 16 Streamwise velocity distributions
at several streamwise stations
downstream of the blade trailing
edge